RSC Advances

PAPER

Cite this: *RSC Adv.*, 2015, **5**, 43130

A flexible free-standing defect-rich MoS_2/graphene/carbon nanotube hybrid paper as a binder-free anode for high-performance lithium ion batteries†

Longsheng Zhang, Wei Fan and Tianxi Liu*

Received 22nd March 2015
Accepted 7th May 2015

DOI: 10.1039/c5ra05038c

www.rsc.org/advances

The rapid development of flexible energy storage devices has motivated people to seek reliable electrodes with both high mechanical flexibility and excellent electrochemical performance. Herein, we demonstrate a facile and scalable process to fabricate a flexible free-standing defect-rich MoS_2/graphene/carbon nanotube (dr-MGC) hybrid paper, which can be directly used as a flexible binder-free anode for lithium ion batteries. Benefiting from the excellent dispersibility of defect-rich MoS_2 nanosheets (dr-MoS_2 NSs) and graphene oxide/carbon nanotube (GO/CNT) hybrids in aqueous solution, a unique three-dimensional (3D) nanoporous architecture with ultrathin dr-MoS_2 NSs homogeneously embedded in graphene/CNT frameworks is nicely constructed by a simple vacuum filtration and thermal reduction process. As a consequence, the flexible free-standing dr-MGC21 hybrid paper exhibits a high reversible capacity of 1137.2 mA h g^{-1} at a current density of 0.1 A g^{-1} with excellent cyclic stability and rate capability. The superior electrochemical performance of the dr-MGC hybrid paper is ascribed to the 3D nanoporous architecture as well as the synergistic effect between the dr-MoS_2 NSs and conductive graphene/CNT network. Moreover, the idea of utilizing graphene/CNT hybrids as flexible conductive frameworks provides a novel pathway for the large-scale fabrication of various flexible binder-free electrodes for high-performance flexible energy storage devices.

1. Introduction

Lithium ion batteries (LIBs) have become one of the main energy storage devices for applications in portable electronics and electric vehicles, due to their high energy density, long cycling life and environmental benignity.[1–3] Recently, the great interest in portable and flexible electronics has created a strong driving force for the development of lightweight and flexible LIBs with high lithium storage capacity.[4–6] In order to fulfill this demand, it is urgently needed to explore reliable electrode materials and develop efficient assembly approaches for the fabrication of flexible electrodes with robust mechanical property and excellent electrochemical performance.[7] However, the conventional approach to fabricate flexible electrodes includes mixing the anode materials with conductive agents and polymer binders and then coating the mixture on a flexible substrate, which is complicated and time-consuming.[8] Besides, the polymer binders are insulating and electrochemically inert, which may block the diffusion channels for lithium ion transport and severely decrease the overall energy and power density of the electrodes.[9] Therefore, binder-free electrodes with high mechanical flexibility, superior reversible capacity and cyclic stability are highly desirable for the development of high-performance flexible energy storage devices.[10–13]

Recently, graphene has attracted tremendous attention as a promising electrode material in energy storage applications owing to its unique properties including excellent mechanical properties, large specific surface area and superior electronic conductivity.[14–16] More importantly, graphene can be easily assembled into flexible self-standing paper-like materials, which can be directly used as flexible binder-free electrodes in energy storage devices.[17–20] It has been reported that free-standing graphene papers demonstrate better mechanical stiffness and strength than other paper-like carbonaceous materials, *e.g.* carbon nanotube (CNT) paper or graphite foil.[21,22] Additionally, free-standing graphene paper can not only act as a conducting agent, but also as a current collector, which is an ideal base material for fabricating flexible binder-free electrode.[23,24] However, irreversible aggregation of graphene sheets due to the strong interlayer π–π stacking and van der Waals interaction could seriously prevent lithium ions from accessing the surface area and result in decreased lithium storage capacity.[25,26] To alleviate this issue, an efficient strategy is to

State Key Laboratory of Molecular Engineering of Polymers, Department of Macromolecular Science, Fudan University, 220 Handan Road, Shanghai 200433, P. R. China. E-mail: txliu@fudan.edu.cn; Fax: +86-21-65640293; Tel: +86-21-55664197

† Electronic supplementary information (ESI) available. See DOI: 10.1039/c5ra05038c

incorporate CNTs between graphene sheets to form sandwich-type structures, which can effectively prevent the re-stacking of graphene sheets.[27–32] By utilizing CNTs as spacers, conductive linkers as well as mechanical reinforcement, the interconnected graphene/CNT network exhibits enhanced porosity, electrical conductivity and mechanical properties.[33–35] Nevertheless, most of the previous work on graphene/CNT hybrids includes incorporation of surfactant which impairs the conductivity,[36] or tedious preparation method such as chemical vapor deposition.[37] In this regard, our group has reported a simple and efficient approach to utilize graphene oxide (GO) as versatile dispersants to directly stabilize pristine CNTs in aqueous media through mild sonication.[27] The resulting homogenous GO/CNT hybrid dispersion with excellent stability is crucial for fabricating flexible self-standing graphene/CNT-based hybrid papers *via* vacuum-assisted self-assembly. Furthermore, graphene/CNT hybrids can provide a three-dimensional (3D) flexible conductive framework with large specific surface area for further incorporation of active materials (*e.g.* metal oxides, metal sulfides, *etc.*) with higher specific capacity.[38–40] Therefore, it is expected to be an efficient assembly approach to fabricate high-performance graphene/CNT-based flexible electrodes by employing GO/CNT hybrids and electrochemically active materials as co-building blocks.

Among various kinds of potential active materials, molybdenum disulfide (MoS_2) has been considered as a promising electrode material for high-performance LIBs due to its unique properties and high theoretical specific capacity ($\sim$669 mA h g^{-1}).[41] As a typical layered transition metal sulfide, MoS_2 has a structure analogous to that of graphite, in which three stacked atom layers (S–Mo–S) are held together through van der Waals interactions.[42] Nevertheless, MoS_2 is prone to form two-dimensional lamellar structure and its preferentially exposed surfaces are the thermodynamically stable basal planes instead of the electrochemically active edge planes.[43,44] Therefore, introducing abundant defects into the surface of MoS_2 could form cracks on its basal planes and subsequently increase the exposure of active edge sites.[45] Recently, ultrathin defect-rich MoS_2 nanosheets (dr-MoS_2 NSs) with exposure of additional active edge sites have been successfully prepared *via* a simple one-step hydrothermal method, leading to significantly improved electrocatalytic performances.[46] However, the practical applications of MoS_2 as anode materials are severely hindered by its poor cyclic stability and inferior rate performance, which originates from the intrinsic poor electric/ionic conductivity between two adjacent S–Mo–S layers.[47] To overcome this disadvantage, constructing hierarchical hybrid structures of nanostructured MoS_2 with conductive carbonaceous materials (*e.g.* graphene, CNTs) is an effective strategy to improve the electrical conductivity and structural stability of electrode materials.[48–51]

Herein, we present a facile approach to fabricate flexible free-standing dr-MoS_2 NSs/graphene/CNT (dr-MGC) hybrid paper by employing GO/CNT hybrids and dr-MoS_2 NSs as co-building blocks *via* vacuum-assisted self-assembly, which can be directly used as a flexible binder-free anode for LIBs. Benefiting from the excellent dispersibility and morphological compatibility of GO/CNT hybrids and dr-MoS_2 NSs, a unique 3D nanoporous architecture with dr-MoS_2 NSs homogeneously embedded in graphene/CNT frameworks is ingeniously constructed. In the dr-MGC hybrid paper thus designed and prepared, firstly, the ultrathin dr-MoS_2 NSs with exposure of additional active edge sites can greatly facilitate the intercalation of lithium ions, thus resulting in enhanced lithium storage capacity. Secondly, the interconnected graphene/CNT network not only provides highly conductive pathways facilitating the rapid transfer of both lithium ions and electrons, but also accommodates the volumetric expansion of dr-MoS_2 NSs and maintains the structural stability of the overall dr-MGC hybrid paper. Last but not least, by utilizing CNTs as both the spacers and conductive linkers between individual graphene sheets, the graphene/CNT-based hybrid paper exhibits enhanced porosity and electrical conductivity in comparison with bare graphene-based hybrid paper. Owing to the 3D nanoporous architectures as well as the synergistic effect between dr-MoS_2 NSs and graphene/CNT network, the dr-MGC21 hybrid paper demonstrates high reversible capacity of 1137.2 mA h g^{-1} at a current density of 0.1 A g^{-1} with excellent cyclic stability and rate capability. Furthermore, the idea of utilizing graphene/CNT hybrids as flexible conductive frameworks can be applied to immobilization and accommodation of various other electrochemically active materials (*e.g.* metal oxides, metal sulfides, *etc.*), which shows great potential for the large-scale fabrication of flexible binder-free electrodes for high-performance flexible energy storage devices.[52]

2. Experimental section

2.1. Materials

Natural graphite powder (325 meshes) was purchased from Alfa-Aesar. Pristine carbon nanotubes (CNTs) were supplied by Chengdu Institute of Organic Chemistry, Chinese Academy of Sciences. All the other reagents were purchased from Sinopharm Chemical Reagent Co. Ltd. and used as received without further purification. Deionized (DI) water was used throughout all the experiments.

2.2. Synthesis of MoS_2 nanosheets

Defect-rich MoS_2 nanosheets (dr-MoS_2 NSs) were synthesized *via* a facile one-step hydrothermal method according to the procedures reported elsewhere.[46] Typically, 1 mmol hexaammonium heptamolybdate tetrahydrate ($(NH_4)_6Mo_7O_{24}\cdot 4H_2O$) and 30 mmol thiourea ($N_2H_4CS$) were dissolved in 35 mL water under vigorous stirring to form a homogeneous solution. The mixture solution was then sealed in a 45 mL Teflon-lined stainless steel autoclave and hydrothermally treated at 220 °C for 18 h. Finally, the as-prepared black precipitate was washed with water and absolute ethanol for several times and dried at 60 °C under vacuum. For the synthesis of defect-free MoS_2 nanosheets (df-MoS_2 NSs), 1 mmol $(NH_4)_6Mo_7O_{24}\cdot 4H_2O$ (*i.e.* 7 mmol Mo) and 14 mmol thiourea (*i.e.* 14 mmol S) were dissolved in 35 mL water under vigorous stirring to form a homogeneous solution and then the mixture solution was treated by the same hydrothermal procedure.[46]

2.3. Preparation of GO/CNT hybrid suspensions

Stable aqueous suspensions of GO/CNT hybrids were prepared by our method reported previously.[27] Briefly, GO was synthesized from natural graphite powder by a modified Hummers method.[53] The resulting GO solid was dispersed in water by sonication under ambient condition for 30 min to make a homogeneous GO aqueous dispersion. Then pristine CNTs are added into the aqueous colloidal suspension of GO sheets with GO to CNT weight ratio of 2/1, and then the mixture was sonicated for 1 h at room temperature. The mixed suspension was centrifuged for 30 min at 8000 rpm to remove the unstabilized CNTs, thus giving a homogeneous and stable suspension of GO/CNT hybrids.

2.4. Fabrication of dr-MoS_2/graphene/CNT hybrid papers

The flexible free-standing dr-MoS_2/graphene/CNT (dr-MGC) hybrid paper was fabricated through a simple vacuum filtration and thermal reduction process. In a typical procedure, a designed amount of dr-MoS_2 NSs suspension (0.5 mg mL^{-1}) and GO/CNT hybrid suspension (0.5 mg mL^{-1}) were mixed together and sonicated under ambient condition for 1 h. Subsequently, the mixed suspension containing dr-MoS_2 NSs and GO/CNT hybrids was vacuum-filtrated through a poly(vinylidene fluoride) (PVDF) membrane filter (220 nm pore size, Durapore® from Sigma-Aldrich). After peeled off from the membrane filter, the as-fabricated dr-MoS_2/GO/CNT hybrid paper was placed in an alumina crucible and annealed in a conventional tube furnace at 800 °C for 2 h under pure nitrogen gas atmosphere (from which the GO was thermally reduced to graphene). The obtained dr-MGC hybrid papers with dr-MoS_2 NSs to GO/CNT hybrids weight ratios of 1/2, 1/1 and 2/1 were named as dr-MGC12, dr-MGC11 and dr-MGC21, respectively. For the control experiment, bare graphene/CNT (GC) hybrid paper and dr-MoS_2/graphene (dr-MG) hybrid paper were also fabricated by the same procedure without adding dr-MoS_2 NSs or CNTs. Similarly, the dr-MG hybrid paper with dr-MoS_2 NSs to GO weight ratio of 2/1 was named as dr-MG21.

2.5. Materials characterization

Field emission scanning electron microscopy (FESEM) characterization was conducted with Ultra 55 Zeiss FESEM at an accelerating voltage of 5 kV. Transmission electron microscopy (TEM) and high-resolution transmission electron microscopy (HRTEM) observations were performed with Tecnai G2 20 TWIN TEM under an acceleration voltage of 200 kV. All the TEM samples were firstly dispersed in aqueous solutions *via* sonication to form homogenous suspensions. Then the TEM samples were prepared by dropping the suspensions on the copper grids and drying in air. Atomic force microscopy (AFM) images were taken under tapping mode with a Scanning Probe Microscope (SPM) Nanoscope IV from Digital Instruments. X-ray diffraction (XRD) patterns of the samples were conducted on an X'Pert Pro X-ray diffractometer with Cu Kα radiation (λ = 0.1542 nm) under a voltage of 40 kV and a current of 40 mA. X-ray photoelectron spectroscopy (XPS) analyses were made with a VG ESCALAB 220I-XL device. All XPS spectra were corrected using C 1s line at 284.5 eV and the curve fitting was accomplished using XPS Peak 4.1 software.

2.6. Electrochemical measurements

The electrochemical experiments were carried out in 2025 coin-type half-battery cells assembled in an argon-filled glovebox (M. Braun Inertgas Systems Co. Ltd.). Pure lithium foil was used as the counter electrode and Celgard-2400 membrane was used as the separator. The electrolyte was consisted of a solution of 1 M LiPF6 in ethylene carbonate (EC)/dimethyl carbonate (DMC)/diethyl carbonate (DEC) (1 : 1 : 1 by volume). The self-standing dr-MGC, dr-MG and GC hybrid papers were directly used as working electrodes without adding any binders or carbon black. Thus, the capacities of all hybrid papers are calculated based on the total mass of the whole hybrid papers. For comparison, the bare dr-MoS_2 NS electrodes were prepared by a slurry coating procedure. The slurry is consisted of dr-MoS_2 NSs, carbon black and poly(vinylidene fluoride) dissolved in *N*-methyl-2-pyrrolidinone (NMP) at a weight ratio of 8 : 1 : 1. The as-prepared slurry was pasted on pure copper foil and dried at 80 °C under vacuum. For clarification, the capacity of bare dr-MoS_2 NS electrodes is calculated based on the weight of active materials (defined as dr-MoS_2 NS in this work), without including carbon black and poly(vinylidene fluoride). The cells were assembled in an argon-filled glovebox with the concentrations of moisture and oxygen below 0.1 ppm. Cyclic voltammetry (CV) curves were collected on a CHI660C electrochemical workstation (Chenhua Instruments Co. Ltd.) in the potential range from 0.01 to 3.0 V at a scan rate of 0.1 mV s^{-1}. The galvanostatic discharge/charge measurements and rate-performance tests under different current densities were performed in the voltage range from 0.01 to 3.0 V at room temperature by using a CT2013A cell test instrument (LAND Electronic Co. Ltd.). The electrochemical impedance spectroscopy (EIS) was measured in the frequency range from 100 kHz to 0.01 Hz with an AC voltage amplitude of 5.0 mV.

3. Results and discussion

3.1. Structure and morphology of dr-MGC hybrid papers

The structure and morphology of the as-obtained MoS_2 NSs, GO sheets and GO/CNT hybrids were investigated using FESEM, TEM and AFM. As shown in Fig. 1a, the as-prepared dr-MoS_2 NSs are of ultrathin nanosheet morphology with curled edges and their lateral sizes are typically in the range from 100 to 200 nm. In contrast, the commercially bulk MoS_2 tends to agglomerate and their lateral sizes are typically in the range from 500 nm to several micrometers (Fig. S1, see ESI†). From the corresponding TEM image in Fig. 1b, obvious ripples and corrugations can be observed, revealing the ultrathin nature of dr-MoS_2 NSs. The HRTEM image (Fig. 1c) of the curled edges further indicates that dr-MoS_2 NSs exhibit a typical lamellar structure with interlayer spacing of 0.63 nm and a thickness of about 3–5 nm, corresponding to 5–8 sandwiched S–Mo–S layers. Furthermore, as indexed in Fig. 1c, the crystal fringes along the curled edges of dr-MoS_2 NSs are discontinuous, which

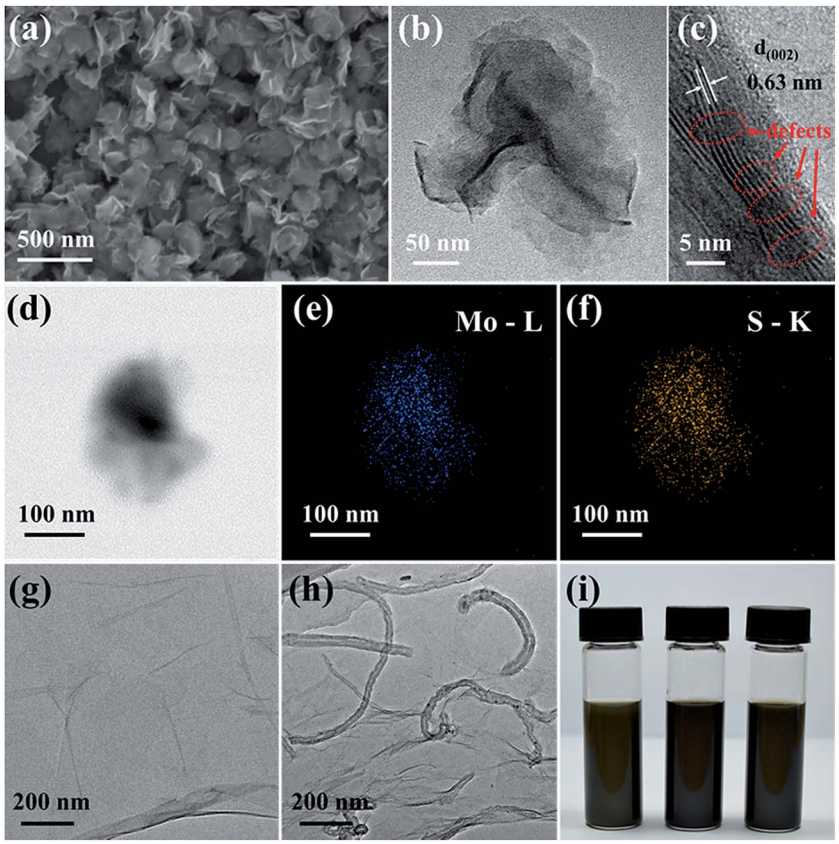

Fig. 1 (a) FESEM, (b) TEM and (c) HRTEM images of dr-MoS_2 NSs. (d)–(f) TEM image and EDS mapping images of dr-MoS_2 NSs. TEM images of (g) GO sheets and (h) GO/CNT hybrids. (i) Digital photos of the dispersions of (left) dr-MoS_2 NSs, (middle) GO/CNT (2/1, w/w) hybrids and (right) the mixture of dr-MoS_2 NSs and GO/CNT hybrids (2/1, w/w) in aqueous solution, respectively. All the dispersions (1 mg mL^{-1}) were stored still for one week before taking photos.

originates from the existence of abundant defects cracking of the basal planes of dr-MoS_2 NSs.[46] Such a defect-rich structure of dr-MoS_2 NSs can enormously increase the exposure of active edge sites owing to the formation of cracks on the basal surface brought by abundant defects. In addition, the TEM image and the corresponding EDS mapping images of dr-MoS_2 NSs (Fig. 1d–f) reveal the homogeneous distribution of molybdenum and sulfur elements in the whole ultrathin nanosheet. In comparison, the df-MoS_2 NSs synthesized *via* a quantitative reaction without excess thiourea exhibit similar ultrathin nanosheet morphology with interlayer spacing of 0.63 nm, but no discontinuous crystal fringes were observed along the curled edges of df-MoS_2 NSs (Fig. S2, see ESI†).

From the TEM image of GO sheets (Fig. 1g), the exfoliated GO sheets are thin and slightly scrolled on sheet edges, similar to those reported previously.[35] The AFM image and the corresponding height profile (Fig. S3, see ESI†) show that the thickness of GO sheets is about 1 nm, revealing that large amounts of oxygen-containing groups are introduced onto the GO sheets during the Hummers oxidation process. Owing to the hydrophilic oxygen groups attached to the GO basal plane and edges (Scheme 1), GO sheets can form a stable aqueous suspension under sonication and be utilized as efficient dispersants to stabilize the pristine CNTs in water. Based on our previous studies, homogeneous aqueous dispersions of GO/CNT hybrids with GO to CNT weight ratio of 2/1 can be facilely obtained, suggesting strong stabilizing ability of GO sheets for pristine CNTs in aqueous media.[27] The TEM image of GO/CNT hybrids (Fig. 1h) exhibits that pristine CNTs are randomly anchored on the surface of GO sheets, which results from the strong interactions between GO sheets and pristine CNTs. During the formation of GO/CNT hybrids, GO sheets can effectively hinder the aggregation of pristine CNTs, while the CNTs can simultaneously prevent the re-stacking of GO sheets. It is supposed that the π-conjugated multiple aromatic regions of GO sheets can interact with the sidewalls of CNTs through the π–π stacking interactions, while the hydrophilic oxygen groups can maintain good water solubility of GO/CNT hybrids. Owing to the strong π–π stacking interactions between GO and CNTs, and abundant hydrophilic oxygen groups of GO sheets, the GO/CNT hybrid suspension is quite stable (Fig. 1i) with only a little amount of unstabilized CNTs after the centrifugation procedure. As shown in Fig. 1i, the aqueous dispersion of dr-MoS_2 NSs is also pretty stable, indicating excellent dispersibility of this sample. Thus, a stable and homogenous mixture dispersion of dr-MoS_2 NSs and GO/CNT hybrids can be readily prepared (right in Fig. 1i), which is advantageous for the fabrication of flexible free-standing dr-MGC hybrid papers.

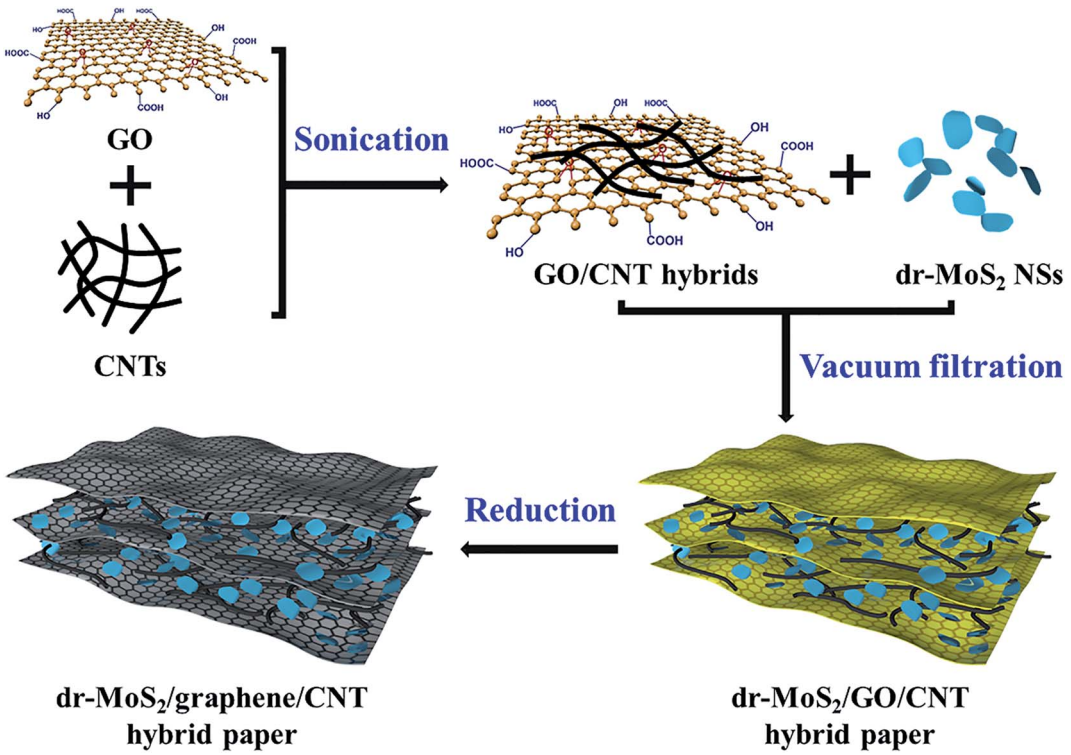

Scheme 1 Schematic illustration of the fabrication of flexible free-standing dr-MoS_2/graphene/CNT hybrid papers.

As illustrated in Scheme 1, flexible self-standing dr-MGC hybrid papers can be easily fabricated through a simple vacuum filtration of the mixed dispersion of dr-MoS_2 NSs and GO/CNT hybrids, followed by the thermal reduction of GO to graphene. The morphology and structure of dr-MGC21 hybrid paper were investigated by FESEM (Fig. 2). The top-view FESEM images of dr-MGC21 hybrid paper at low and high magnifications are displayed in Fig. 2a and b, respectively. It can be clearly observed that ultrathin dr-MoS_2 NSs are homogeneously embedded in the graphene/CNT hybrid frameworks, which can be attributed to the excellent dispersibility of dr-MoS_2 NSs and GO/CNTs hybrids that were used for the vacuum filtration. The average thickness of dr-MGC21 hybrid paper prepared *via* vacuum filtration is about 8 μm as exhibited by the cross-sectional FESEM image at low magnification (Fig. 2c). And the thickness of dr-MGC hybrid paper is tunable, which can be readily obtained by changing the initial amount of the homogenously mixed dispersion of dr-MoS_2 NSs and GO/CNT hybrids during the vacuum filtration process. Furthermore, the insets in Fig. 2a and c show that the dr-MGC21 hybrid paper with diameter of *ca.* 38 mm is free-standing and flexible, which can be bent back and forth without broken. In this study, when the weight ratio of dr-MoS_2 NSs to GO/CNT hybrids ranges from 1/2 to 2/1, the free-standing dr-MGC hybrid papers can be readily obtained. However, it is worthy to mention that further increasing the amount of dr-MoS_2 NSs will result in the fracture of dr-MGC hybrid paper. From the cross-sectional FESEM images at high magnification for dr-MGC21 hybrid paper (Fig. 2d), layered dr-MoS_2 NSs are uniformly incorporated between the large lateral dimensional graphene layers with randomly interspersed CNTs, resulting in 3D nanoporous sandwiched structures. Besides, from the cross-sectional FESEM images of all three dr-MGC hybrid papers (Fig. S4, see ESI†), the weight ratio difference of dr-MoS_2 NSs to graphene/CNT hybrids hasn't changed the 3D nanoporous sandwiched structures of these dr-MGC hybrid papers. Moreover, the content of dr-MoS_2 NSs in the dr-MGC hybrid papers clearly increases with the increasing weight ratio of dr-MoS_2 NSs to graphene/CNT hybrids. Furthermore, the corresponding EDS mapping images of all three dr-MGC hybrid papers reveal the

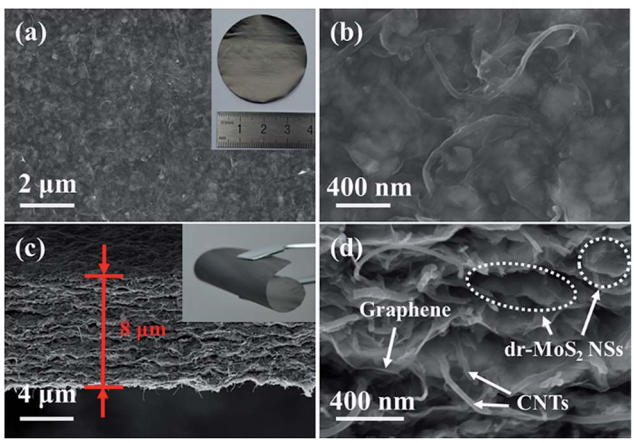

Fig. 2 (a) and (b) Top-view and (c) and (d) cross-sectional FESEM images of dr-MGC21 hybrid paper at low (left) and high (right) magnifications. The insets of (a) and (c) show the digital photos of flexible free-standing dr-MGC21 hybrid paper.

homogeneous distribution of carbon, molybdenum and sulfur elements in the hybrid papers (Fig. S5, see ESI†). These results indicate that ultrathin layered dr-MoS_2 NSs are homogeneously dispersed in the 3D nanoporous graphene/CNT frameworks, which is attributed to the excellent dispersibility of dr-MoS_2 NSs and GO/CNT hybrids in aqueous solution. From the corresponding EDS spectra of all three dr-MGC hybrid papers, four peeks located at 0.27, 0.52, 2.29 and 2.3 keV are observed, corresponding to carbon KR, oxygen KR, molybdenum LR and sulfur KR energy, respectively. These results verify the co-existence of C, Mo, S and O elements in all three dr-MGC hybrid papers without detectable impurity. The low oxygen content reveals that graphene in all three dr-MGC hybrid papers are highly reduced after calcination process. Moreover, from all the three EDS spectra, it can be clearly seen that the content of Mo and S elements in all three dr-MGC hybrid papers increases with the increasing weight ratio of dr-MoS_2 NSs to graphene/CNT hybrids, which is consistent with the morphology analysis of these three hybrid papers. The well-dispersed dr-MoS_2 NSs expand the interlayer spacing between the graphene layers and prevent their agglomeration, which can facilitate diffusion kinetics of lithium ions in the electrode. Simultaneously, the graphene sheets interconnected by the CNTs not only effectively hinder dr-MoS_2 NSs from aggregation, but also provide 3D conductive networks with robust mechanical properties. Moreover, the confinement of dr-MoS_2 NSs within graphene/CNT frameworks can greatly inhibit the volumetric expansion of dr-MoS_2 NSs during the lithiation/delithiation process. Here, the CNTs can act as both the spacers and conductive linkers between individual graphene layers, which can further prevent the re-stacking of graphene sheets, leading to higher porosity and conductivity. In contrast, the dr-MG21 hybrid paper without any CNTs has a much more compact sandwiched structure (Fig. S6, see ESI†). From the BET analysis, the specific surface area of dr-MGC21 and dr-MG21 are 118.5 and 76.3 $m^2 g^{-1}$, respectively, which directly verifies that the incorporation of CNTs can increase the porosity and specific surface area of hybrid papers (Fig. S7, see ESI†). The pore size distribution of the dr-MGC21 hybrid paper calculated from the Barrett–Joyner–Halenda (BJH) method is mainly centered at about 4 nm, which is in the mesoporous range (inset of Fig. S7†). Therefore, owing to the synergistic effect between the ultrathin dr-MoS_2 NSs and the graphene/CNT frameworks, the resulting dr-MGC hybrid papers possess 3D nanoporous structures with high mechanical flexibility.

The detailed microstructures of the dr-MGC21 hybrid paper were further investigated by TEM observations (Fig. 3a and b). It can be clearly seen that pristine CNTs are randomly anchored on the surface of graphene sheets while layered dr-MoS_2 NSs are homogeneously confined in the graphene/CNT network, which is consistent with the FESEM observations. Notably, the incorporation of CNTs and dr-MoS_2 NSs can efficiently prevent the re-stacking of graphene sheets, thus leading to full utilization of high-surface-area graphene sheets. Besides, the strong interactions between graphene sheets and CNTs enable the rapid charge transfer for improving the electrical conductivity of overall dr-MGC21 hybrid paper. Furthermore, the morphological compatibility between two dimensional dr-MoS_2 NSs and graphene sheets can increase the electrical contact areas for rapid transfer of lithium ions and electrons across the interface, which could significantly improve the electrochemical performances. From the EDX spectra of the circled region (Fig. 3c), two peaks located at 0.27 and 0.52 keV are observed, corresponding to carbon and oxygen KR energy, respectively.[54] The low oxygen content reveals that graphene sheets in the dr-MGC21 hybrid paper are highly reduced. As for the EDX spectra of the squared area (Fig. 3d), the peaks corresponding to Mo and S are prominent in comparison with that of carbon, which unambiguously verifies the presence of dr-MoS_2 NSs in the dr-MGC21 hybrid paper.

The XRD patterns of GO, CNTs, GO/CNT hybrids, GC hybrid paper, dr-MoS_2 NSs and dr-MGC21 hybrid paper are shown in Fig. 4. GO shows a typical diffraction peak at $2\theta = 10.6^\circ$ due to the introduction of oxygen-containing groups on graphene sheets, and pristine CNTs displays a characteristic diffraction peak at $2\theta = 26.2^\circ$. Two obvious diffraction peaks at $2\theta = 10.6^\circ$ and 26.2° are observed in the XRD pattern of GO/CNT hybrids, which indicates the co-existence of GO and CNTs. For GC hybrid paper, the diffraction peak at $2\theta = 10.6^\circ$ disappears, suggesting the successful reduction of GO sheets after the thermal reduction process. Four diffraction peaks located at $2\theta = 14.2^\circ$, 33.5°, 39.6° and 59.3° are observed for bare dr-MoS_2 NSs, which can be indexed to (002), (100), (103) and (110) planes of MoS_2 (JCPDS 37-1492). The dr-MGC21 hybrid paper shows the combination of both GC and dr-MoS_2 NSs while no obvious peaks from the impurity phase are observed, indicating the co-existence of graphene, CNTs and dr-MoS_2 NSs in the dr-MGC21 hybrid paper. Besides, as shown in Fig. S8 (see ESI†), the XRD patterns of all three dr-MGC hybrid papers display the combination of both graphene/CNT hybrids and dr-MoS_2 NSs components, indicating the co-existence of graphene/CNT hybrids and dr-MoS_2 NSs. Moreover, the intensity of all the diffraction peaks belonging to dr-MoS_2 NSs gradually increases as the amount of dr-MoS_2 NSs in the dr-MGC hybrid papers increases.

XPS analysis (Fig. 5) was performed to further confirm the surface electronic state and composition of dr-MGC21 hybrid paper. Fig. 5a reveals the existence of C, Mo, S and O elements in the as-fabricated dr-MGC21 hybrid paper, and no detectable impurity is observed. Fig. 5b displays the high resolution Mo 3d spectrum of dr-MGC21 hybrid paper in the binding energy range of 222–240 eV. Two peaks located at 229.4 eV and 232.7 eV can be ascribed to Mo $3d_{5/2}$ and Mo $3d_{3/2}$ binding energies respectively, which is characteristic of Mo^{4+} in MoS_2, indicating the dominance of Mo(IV) in the dr-MGC21 hybrid paper. Additionally, a small peak located at 226 eV can be observed, corresponding to S 2s component of MoS_2. From the high resolution S 2p spectrum (Fig. 5c), two peaks at 163.3 eV and 162.2 eV can be observed, which are attributed to S $2p_{1/2}$ and S $2p_{3/2}$ orbitals of divalent sulfide ions (S^{2-}), respectively. These results are consistent with those reported previously for MoS_2 NSs.[50] From the C 1s spectra of GO/CNT hybrids (Fig. S9, see ESI†), five different peaks centered at 284.5, 285.6, 286.7, 287.8 and 288.8 eV are observed, corresponding to sp^2 C, sp^3 C, –C–O, –C═O and –COO– groups, respectively.[55] In comparison with

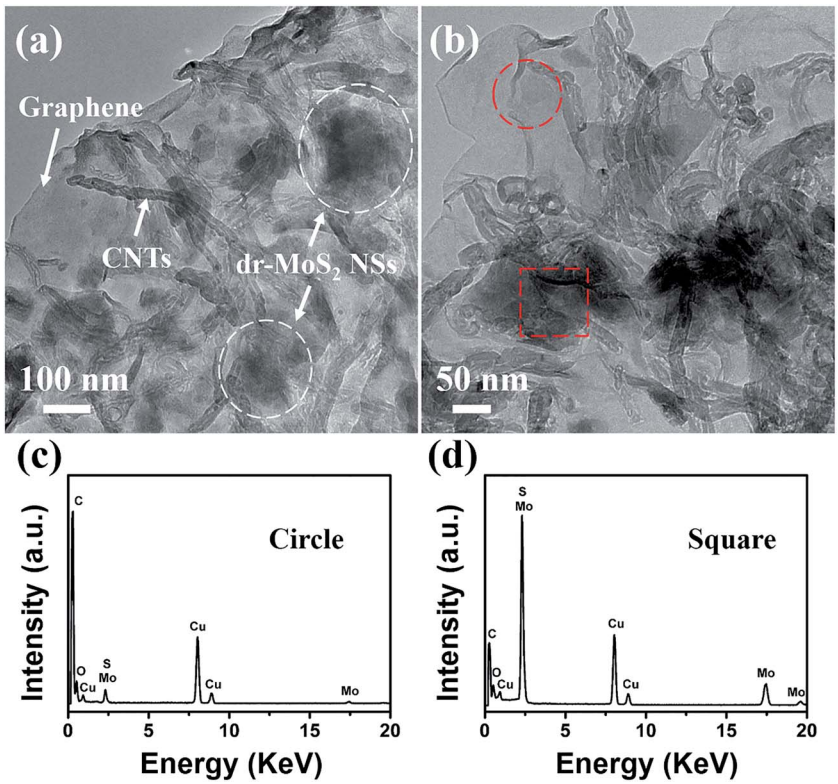

Fig. 3 TEM images of dr-MGC21 hybrid paper at (a) low and (b) high magnifications. (c) and (d) The corresponding EDX spectra of circled and squared areas indicated in the TEM image.

GO/CNT hybrids, the intensities of C 1s peaks of the carbons binding to oxygen (–C–O, –C═O and –COO– groups) remarkably decrease for dr-MGC21 hybrid paper (Fig. 5d), suggesting that most of the oxygen-containing functional groups are removed after the thermal reduction process.

3.2. Electrochemical performance of dr-MGC hybrid papers

Coin cells were assembled to evaluate the electrochemical performance of dr-MGC hybrid papers and bare MoS_2 NSs as anode materials for LIBs. The flexible free-standing dr-MGC hybrid papers were directly used as working electrode without adding any binders or conducting additive. Fig. 6a shows the CV curves of the first three cycles of dr-MGC21 hybrid paper measured at a scan rate of 0.1 mV s^{-1} in the voltage range from 0.01 to 3.0 V. There are two reduction peaks located at 1.10 and 0.45 V and two oxidation peaks located at 1.73 and 2.27 V in the first CV cycle for dr-MGC21 hybrid paper. The first reduction peak located at 1.10 V can be attributed to Li insertion into defect sites of dr-MoS_2 NSs, forming Li_xMoS_2 according to the literature.[56] The pronounced reduction peak at 0.45 V corresponds to the reduction of Li_xMoS_2 into Mo nanoparticles embedded in Li_2S matrix.[57] During the anodic scan, the small oxidation peak at 1.73 V should be ascribed to the reversible lithium storage on graphene sheets and CNTs since it is absent in the CV curves of dr-MoS_2 NSs (Fig. S10, see ESI†). The strong oxidation peak at 2.27 V is associated with the oxidation of Li_2S into S *via* a conversion reaction.[58] In the subsequent cycles, the reduction peaks observed at 1.10 V and 0.45 V disappear with emergence of two new peaks at 1.95 V and 1.27 V, suggesting the multistep lithiation process of S to form Li_2S.[56] As for bare dr-MoS_2 NSs, the CV profile (Fig. S10, see ESI†) in the first cycle is similar to that of dr-MGC21 hybrid paper. However, the intensities of oxidation peaks at 2.36 V obviously decrease during the subsequent cycles, suggesting a poor cyclic stability of the dr-MoS_2 NS electrode. In comparison, for the dr-MGC21 hybrid paper, CV curves of the subsequent cycles are almost overlapped, indicating a good reversibility during the lithiation/delithiation process.

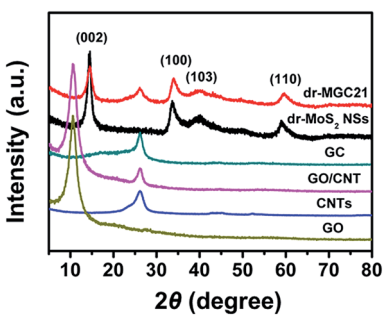

Fig. 4 XRD patterns of GO, CNTs, GO/CNT hybrids, GC, dr-MoS_2 NSs and dr-MGC21 hybrid paper.

Fig. 6b displays the initial discharge/charge curves of bare dr-MoS_2 NSs and the dr-MGC hybrid papers with various dr-MoS_2 contents measured at a current density of 0.1 A g^{-1} in

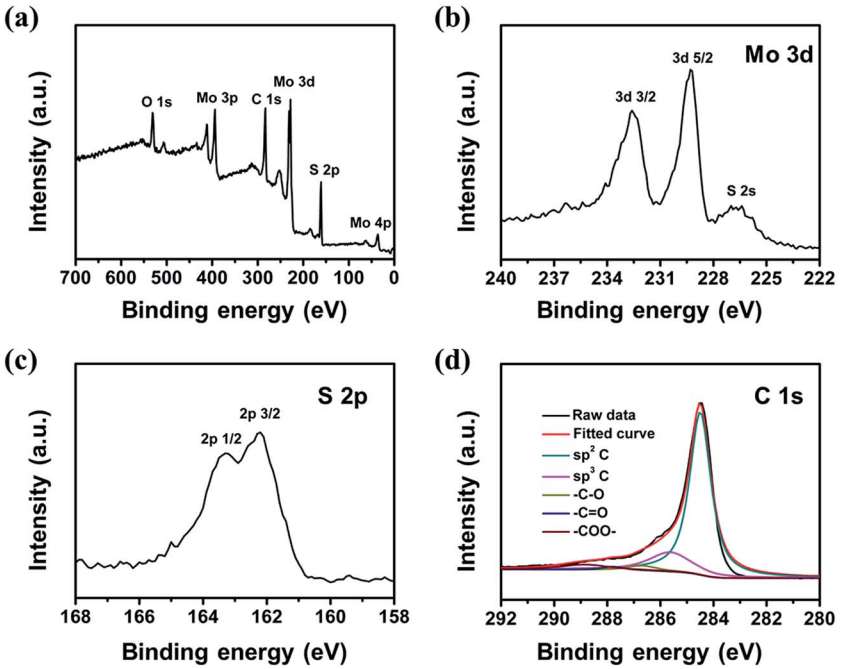

Fig. 5 (a) XPS survey spectrum, high resolution (b) Mo 3d spectrum, (c) S 2p spectrum and (d) C 1s spectrum of dr-MGC21 hybrid paper.

the voltage range from 0.01 to 3.0 V. For all these samples, there are two potential plateaus located at 1.2 and 0.6 V in the discharge curves and two plateaus at 1.7 and 2.2 V in the charge curves, indicating the multistep lithiation/delithiation process of dr-MoS_2 NSs, which is consistent with the CV results. In the first cycle, bare dr-MoS_2 NSs deliver a charge capacity of 715.2 mA h g^{-1}, while the dr-MGC12, dr-MGC11 and dr-MGC21 hybrid papers exhibit much enhanced charge capacities of 756.9, 926.8 and 1137.2 mA h g^{-1}, respectively. The greatly improved lithium storage capacities of the hybrid papers can be attributed to the 3D conductive graphene/CNT frameworks incorporated in the dr-MGC hybrid papers, which provide highly conductive pathways facilitating the rapid transfer of both lithium ions and electrons. Besides, the capacity of dr-MoS_2 NSs are compromised due to the involvement of polymer binders during the electrode preparation, which are

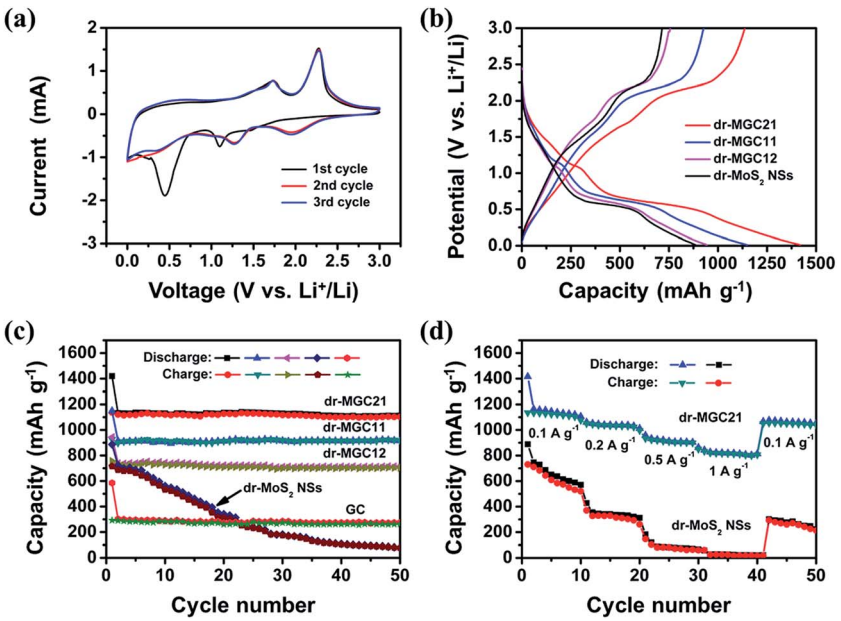

Fig. 6 (a) First three cycles of CV curves of dr-MGC21 hybrid paper measured at a scan rate of 0.1 mV s^{-1}. (b) The initial discharge/charge curves of dr-MoS_2 NSs and dr-MGC hybrid papers. (c) Cycling performance of GC, dr-MoS_2 NSs and dr-MGC hybrid papers in the voltage range from 0.01 to 3.0 V at a current density of 0.1 A g^{-1}. (d) Rate performance of dr-MoS_2 NSs and dr-MGC21 hybrid at various current densities.

insulating and electrochemically inert and severely decrease the overall lithium storage capacity. By comparison, the binder-free property of dr-MGC hybrid papers can fully realize the potential of dr-MoS_2 NSs and lead to greatly enhanced lithium storage capacity. Among all these hybrid papers, the dr-MGC21 hybrid paper presents the highest initial charge capacities, implying the importance of optimizing the weight ratio of dr-MoS_2 NSs to graphene/CNT hybrids in the hybrid paper. However, further increasing the amount of dr-MoS_2 NSs will lead to the fracture of the hybrid paper. Therefore, only with the optimum weight ratio of dr-MoS_2 NSs to graphene/CNT hybrids, the dr-MGC hybrid paper can achieve the best electrochemical performance while maintaining robust mechanical properties simultaneously.

Fig. 6c shows the cycling performance of GC, dr-MoS_2 NSs and dr-MGC hybrid papers with various dr-MoS_2 contents at a current density of 0.1 A g^{-1}. Although the bare GC hybrid paper shows excellent cycling stability, it only delivers a charge capacity of about 270 mA h g^{-1}. On the contrary, the cycling stability of bare dr-MoS_2 NSs is so inferior that the reversible capacity dramatically decreases to 174.5 mA h g^{-1} after 30 cycles and only remains at 79.8 mA h g^{-1} after 50 cycles. Notably, the reversible capacity of bare dr-MoS_2 NSs is generally higher than those of bare df-MoS_2 NSs and bulk MoS_2, even though they all show continuous capacity fading during the cycling process (Fig. S11, see ESI†). The enhanced capacity of dr-MoS_2 NSs is attributed to the abundant defects cracking of the basal planes of dr-MoS_2 NSs, which greatly enhances the accessibility of internal surface areas and exposes much more active edge sites for the intercalation of lithium ions. In comparison with bare dr-MoS_2 NSs, the dr-MGC12, dr-MGC11 and dr-MGC21 hybrid papers manifest better cyclic stability and exhibit higher reversible capacities of 702.9, 916.8 and 1102.6 mA h g^{-1} after 50 cycles, respectively. This can be attributed to the incorporation of graphene/CNT frameworks in the dr-MGC hybrid papers, which not only significantly enhances the specific capacities but also improves their cyclic stabilities. Moreover, even after the cycling process, the dr-MGC21 hybrid paper remains its 3D nanoporous sandwiched structure with CNTs randomly incorporated between the large lateral dimensional graphene layers (Fig. S12, see ESI†). The inset of Fig. S12† shows that the average thickness of dr-MGC21 hybrid paper after the cycling process is still about 8 μm. The 3D nanoporous graphene/CNT frameworks is very stable, which is advantageous for accommodation of electrochemically active materials (dr-MoS_2 NSs) and maintaining the structural stability of the entire dr-MGC hybrid papers. The nanoporous structure of the dr-MGC hybrid papers can also accommodate the volumetric expansion of dr-MoS_2 NS during the lithiation/delithiation process and thus stabilize the structure of the entire hybrid papers. As shown in Fig. S13 (see ESI†), the dr-MGC21 hybrid paper generally exhibits higher reversible capacities than the dr-MG21 hybrid paper without CNTs, indicating the significance of conductive CNTs incorporated between the graphene sheets. The incorporation of CNTs can not only enhance the electrical conductivity by forming efficient conductive pathways but also increase the porosity within the hybrid paper for rapid diffusion of electrolyte to access active material, thus leading to greatly improved lithium storage capacity.

Fig. 6d shows the rate capability of dr-MoS_2 NSs and dr-MGC21 hybrid paper tested at various current densities. When the current density increases to 0.2, 0.5 and 1 A g^{-1}, the dr-MGC21 hybrid paper delivers a reversible capacity of about 1030, 910 and 680 mA h g^{-1}, respectively. Moreover, it is noteworthy that the dr-MGC21 hybrid can still regain a high reversible capacity of about 1040 mA h g^{-1} (about 90% of the initial charge capacity) when the current density drops back to 0.1 A g^{-1} after cycling under high current densities. As for the bare dr-MoS_2 NSs, the reversible capacity decays to about 20 mA h g^{-1} at the current density of 1 A g^{-1} and only retains a capacity of about 210 mA h g^{-1} (about 30% of the initial capacity) in the first cycle when the current density returns to 0.1 A g^{-1}. Furthermore, obvious capacity fading can be observed for bare dr-MoS_2 NSs after the current density decreases back to 0.1 A g^{-1}. In contrast, the extraordinary cycling stability of the dr-MGC21 hybrid paper is exhibited at various current densities. The high reversible capacity, excellent cycle stability and rate capability of dr-MGC21 hybrid paper could be attributed to the following synergistic effects between the ultrathin dr-MoS_2 NSs and the conductive graphene/CNT network: (1) the ultrathin dr-MoS_2 NSs with exposure of additional active edge sites can significantly facilitate the intercalation of lithium ions and lead to enhanced specific capacity. (2) These ultrathin dr-MoS_2 NSs are homogeneously embedded in the graphene/CNT frameworks, which maintains the structural stability of the entire hybrid paper by accommodating the volumetric expansion of dr-MoS_2 NSs and inhibiting their agglomeration and restacking. (3) The interconnected graphene/CNT network can provide highly conductive pathways facilitating the kinetics for charge transfer and lithium ion transport throughout the dr-MGC hybrid paper, which leads to enhanced electrochemical kinetics of lithium storage. (4) The well-dispersed dr-MoS_2 NSs expand the interlayer spacing between the graphene layers and prevent their agglomeration, and the 3D integrated nanoporous architecture derived from dr-MoS_2 NSs and graphene/CNT hybrids can provide open and continuous channels for rapid diffusion of lithium ions to access active materials. Therefore, the conductive graphene/CNT network, the abundant active edge sites of dr-MoS_2 NSs as well as the overall 3D nanoporous architecture of dr-MGC hybrid papers together contribute to the enhanced electrochemical performance for lithium storage.

In order to further understand the enhanced electrochemical performance of dr-MGC hybrid paper in comparison with bare dr-MoS_2 NSs, EIS measurements were carried out in a frequency range from 100 kHz to 0.01 Hz. Fig. 7 displays the Nyquist plots of the dr-MGC21 hybrid paper and bare dr-MoS_2 NSs after 5 cycles. It clearly shows that the radius of the semicircle for dr-MGC21 hybrid paper in the high frequency region is much smaller than that of bare dr-MoS_2 NSs, indicating that the dr-MGC21 hybrid paper has much lower electron-transfer resistance.[59] These results further confirm that the combination with graphene/CNT network can significantly enhance the electrical conductivity of the dr-MGC hybrid paper and greatly facilitate the electron transport during the lithiation/delithiation

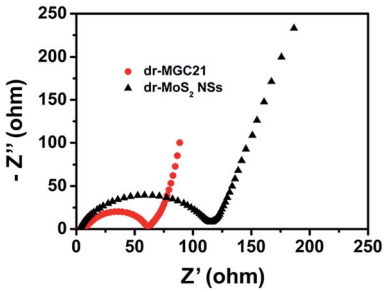

Fig. 7 Nyquist plots of dr-MoS_2 NSs and dr-MGC21 hybrid paper in a frequency range from 100 kHz to 0.01 Hz with an AC voltage amplitude of 5 mV.

process, resulting in significant improvement in the electrochemical performance. As exhibited in Fig. S14 (see ESI†), the diameter of the semicircle at high frequencies for dr-MGC21 hybrid paper is clearly smaller than that of the dr-MG21 hybrid paper without any CNTs, implying greatly decreased charge-transfer resistance at the electrode/electrolyte interface due to the incorporation of CNTs. The conductive CNTs incorporated between the graphene sheets serve as conductive linkers to form an electrically conductive interconnected network, which further facilitates the electrochemical kinetics for both charge and lithium ion transfer throughout the dr-MGC hybrid paper, thus leading to enhanced lithium storage performance.

4. Conclusions

In summary, a facile and scalable process has been developed to fabricate flexible free-standing dr-MGC hybrid paper by employing GO/CNT hybrids and dr-MoS_2 NSs as co-building blocks through a simple vacuum filtration, followed by a thermal reduction process. The resulting dr-MGC hybrid papers with 3D nanoporous architecture provide open and continuous channels for rapid diffusion of lithium ions to access active materials. The ultrathin dr-MoS_2 NSs with exposure of additional active edge sites can facilitate the intercalation of lithium ions, thus leading to enhanced specific capacity. The interconnected graphene/CNT hybrids can provide a conductive framework with large specific surface area for accommodation of dr-MoS_2 NSs, which greatly enhances the electrical conductivity and maintains the structural stability of the overall dr-MGC hybrid paper. Benefiting from the synergetic effect between dr-MoS_2 NSs and graphene/CNT network, the dr-MGC21 hybrid paper with high flexibility exhibits high reversible capacity of 1137.2 mA h g^{-1} at a current density of 0.1 A g^{-1}, with excellent cyclic stability and rate capability. Therefore, this work highlights the great potential of utilizing graphene/CNT hybrids as flexible conductive frameworks to fabricate various flexible binder-free electrodes for high-performance flexible energy storage devices.

Acknowledgements

The authors are grateful for the financial support from the National Natural Science Foundation of China (51125011, 51433001).

References

1 Z. G. Yang, J. L. Zhang, M. C. W. Kintner-Meyer, X. C. Lu, D. W. Choi, J. P. Lemmon and J. Liu, *Chem. Rev.*, 2011, **111**, 3577–3613.
2 F. Y. Cheng, J. Liang, Z. L. Tao and J. Chen, *Adv. Mater.*, 2011, **23**, 1695–1715.
3 P. G. Bruce, B. Scrosati and J. M. Tarascon, *Angew. Chem., Int. Ed.*, 2008, **47**, 2930–2946.
4 H. Nishide and K. Oyaizu, *Science*, 2008, **319**, 737–738.
5 G. M. Zhou, F. Li and H. M. Cheng, *Energy Environ. Sci.*, 2014, **7**, 1307–1338.
6 L. Li, Z. Wu, S. Yuan and X. B. Zhang, *Energy Environ. Sci.*, 2014, **7**, 2101–2122.
7 N. Li, G. M. Zhou, F. Li, L. Wen and H. M. Cheng, *Adv. Funct. Mater.*, 2013, **23**, 5429–5435.
8 C. X. Lu, W. W. Liu, H. Li and B. K. Tay, *Chem. Commun.*, 2014, **50**, 3338–3340.
9 Y. W. Cheng, S. T. Lu, H. B. Zhang, C. V. Varanasi and J. Liu, *Nano Lett.*, 2012, **12**, 4206–4211.
10 Y. T. Liu, X. D. Zhu, Z. Q. Duan and X. M. Xie, *Chem. Commun.*, 2013, **49**, 10305–10307.
11 C. Wang, W. Wan, Y. H. Huang, J. T. Chen, H. H. Zhou and X. X. Zhang, *Nanoscale*, 2014, **6**, 5351–5358.
12 X. L. Jia, Z. Chen, A. Suwarnasarn, L. Rice, X. L. Wang, H. Sohn, Q. Zhang, B. M. Wu, F. Wei and Y. F. Lu, *Energy Environ. Sci.*, 2012, **5**, 6845–6849.
13 L. B. Hu, H. Wu, F. La Mantia, Y. A. Yang and Y. Cui, *ACS Nano*, 2010, **4**, 5843–5848.
14 Y. Q. Sun, Q. Wu and G. Q. Shi, *Energy Environ. Sci.*, 2011, **4**, 1113–1132.
15 C. Rao, A. K. Sood, K. S. Subrahmanyam and A. Govindaraj, *Angew. Chem., Int. Ed.*, 2009, **48**, 7752–7777.
16 X. Huang, Z. Y. Yin, S. X. Wu, X. Y. Qi, Q. Y. He, Q. C. Zhang, Q. Y. Yan, F. Boey and H. Zhang, *Small*, 2011, **7**, 1876–1902.
17 J. Zhang, F. Zhao, Z. P. Zhang, N. Chen and L. T. Qu, *Nanoscale*, 2013, **5**, 3112–3126.
18 Y. Liu, W. Wang, L. Gu, Y. W. Wang, Y. L. Ying, Y. Y. Mao, L. W. Sun and X. S. Peng, *ACS Appl. Mater. Interfaces*, 2013, **5**, 9850–9855.
19 R. H. Wang, C. H. Xu, J. Sun, L. Gao and C. C. Lin, *J. Mater. Chem. A*, 2013, **1**, 1794–1800.
20 R. H. Wang, C. H. Xu, J. Sun, Y. Q. Liu, L. Gao and C. C. Lin, *Nanoscale*, 2013, **5**, 6960–6967.
21 H. Q. Chen, M. B. Mueller, K. J. Gilmore, G. G. Wallace and D. Li, *Adv. Mater.*, 2008, **20**, 3557–3561.
22 D. A. Dikin, S. Stankovich, E. J. Zimney, R. D. Piner, G. Dommett, G. Evmenenko, S. T. Nguyen and R. S. Ruoff, *Nature*, 2007, **448**, 457–460.
23 H. Gwon, H. S. Kim, K. U. Lee, D. H. Seo, Y. C. Park, Y. S. Lee, B. T. Ahn and K. Kang, *Energy Environ. Sci.*, 2011, **4**, 1277–1283.
24 K. Han, Z. Liu, H. Ye and F. Dai, *J. Power Sources*, 2014, **263**, 85–89.
25 C. K. Chua and M. Pumera, *Chem. Soc. Rev.*, 2014, **43**, 291–312.

26 H. R. Byon, B. M. Gallant, S. W. Lee and Y. Shao-Horn, *Adv. Funct. Mater.*, 2013, **23**, 1037–1045.

27 C. Zhang, L. L. Ren, X. Y. Wang and T. X. Liu, *J. Phys. Chem. C*, 2010, **114**, 11435–11440.

28 S. Y. Yang, K. H. Chang, H. W. Tien, Y. F. Lee, S. M. Li, Y. S. Wang, J. Y. Wang, C. Ma and C. C. Hu, *J. Mater. Chem.*, 2011, **21**, 2374–2380.

29 Z. D. Huang, B. A. Zhang, S. W. Oh, Q. B. Zheng, X. Y. Lin, N. Yousefi and J. K. Kim, *J. Mater. Chem.*, 2012, **22**, 3591–3599.

30 C. Zhang, S. Huang, W. W. Tjiu, W. Fan and T. X. Liu, *J. Mater. Chem.*, 2012, **22**, 2427–2434.

31 C. Zhang, W. W. Tjiu and T. X. Liu, *Polym. Chem.*, 2013, **4**, 5785–5792.

32 W. Fan, Y. E. Miao, Y. P. Huang, W. W. Tjiu and T. X. Liu, *RSC Adv.*, 2015, **5**, 9228–9236.

33 Q. Cheng, J. Tang, J. Ma, H. Zhang, N. Shinya and L. C. Qin, *Phys. Chem. Chem. Phys.*, 2011, **13**, 17615–17624.

34 X. J. Lu, H. Dou, B. Gao, C. Z. Yuan, S. D. Yang, L. Hao, L. F. Shen and X. G. Zhang, *Electrochim. Acta*, 2011, **56**, 5115–5121.

35 L. W. Peng, Y. Y. Feng, P. Lv, D. Lei, Y. T. Shen, Y. Li and W. Feng, *J. Phys. Chem. C*, 2012, **116**, 4970–4978.

36 Y. H. Hu, X. F. Li, J. J. Wang, R. Y. Li and X. L. Sun, *J. Power Sources*, 2013, **237**, 41–46.

37 H. W. Park, D. U. Lee, Y. L. Liu, J. S. Wu, L. F. Nazar and Z. W. Chen, *J. Electrochem. Soc.*, 2013, **160**, 2244–2250.

38 L. F. Shen, X. G. Zhang, H. S. Li, C. Z. Yuan and G. Z. Cao, *J. Phys. Chem. Lett.*, 2011, **2**, 3096–3101.

39 C. Z. Yuan, L. Yang, L. R. Hou, J. Y. Li, Y. X. Sun, X. G. Zhang, L. F. Shen, X. J. Lu, S. L. Xiong and X. W. Lou, *Adv. Funct. Mater.*, 2012, **22**, 2560–2566.

40 C. Zhu, X. Mu, P. A. van Aken, J. Maier and Y. Yu, *Adv. Energy Mater.*, 2015, **5**, 1401170.

41 T. Stephenson, Z. Li, B. Olsen and D. Mitlin, *Energy Environ. Sci.*, 2014, **7**, 209–231.

42 H. Matte, A. Gomathi, A. K. Manna, D. J. Late, R. Datta, S. K. Pati and C. Rao, *Angew. Chem., Int. Ed.*, 2010, **49**, 4059–4062.

43 J. V. Lauritsen, J. Kibsgaard, S. Helveg, H. Topsoe, B. S. Clausen, E. Laegsgaard and F. Besenbacher, *Nat. Nanotechnol.*, 2007, **2**, 53–58.

44 A. Albu-Yaron, M. Levy, R. Tenne, R. Popovitz-Biro, M. Weidenbach, M. Bar-Sadan, L. Houben, A. N. Enyashin, G. Seifert, D. Feuermann, E. A. Katz and J. M. Gordon, *Angew. Chem., Int. Ed.*, 2011, **50**, 1810–1814.

45 C. B. Roxlo, H. W. Deckman, J. Gland, S. D. Cameron and R. R. Chianelli, *Science*, 1987, **235**, 1629–1631.

46 J. F. Xie, H. Zhang, S. Li, R. X. Wang, X. Sun, M. Zhou, J. F. Zhou, X. W. Lou and Y. Xie, *Adv. Mater.*, 2013, **25**, 5807–5813.

47 X. Huang, Z. Y. Zeng and H. Zhang, *Chem. Soc. Rev.*, 2013, **42**, 1934–1946.

48 K. Chang and W. X. Chen, *ACS Nano*, 2011, **5**, 4720–4728.

49 X. S. Zhou, L. J. Wan and Y. G. Guo, *Chem. Commun.*, 2013, **49**, 1838–1840.

50 Y. M. Shi, Y. Wang, J. I. Wong, A. Tan, C. L. Hsu, L. J. Li, Y. C. Lu and H. Y. Yang, *Sci. Rep.*, 2013, **3**, 2169.

51 Y. H. Hu, X. F. Li, A. Lushington, M. Cai, D. S. Geng, M. N. Banis, R. Y. Li and X. L. Sun, *ECS J. Solid State Sci. Technol.*, 2013, **2**, 3034–3039.

52 L. Sun, W. B. Kong, Y. Jiang, H. C. Wu, K. L. Jiang, J. P. Wang and S. S. Fan, *J. Mater. Chem. A*, 2015, **3**, 5305–5312.

53 W. S. Hummers and R. E. Offeman, *J. Am. Chem. Soc.*, 1958, **80**, 1339.

54 L. David, R. Bhandavat and G. Singh, *ACS Nano*, 2014, **8**, 1759–1770.

55 Z. J. Fan, W. Kai, J. Yan, T. Wei, L. J. Zhi, J. Feng, Y. M. Ren, L. P. Song and F. Wei, *ACS Nano*, 2011, **5**, 191–198.

56 J. Xiao, X. J. Wang, X. Q. Yang, S. D. Xun, G. Liu, P. K. Koech, J. Liu and J. P. Lemmon, *Adv. Funct. Mater.*, 2011, **21**, 2840–2846.

57 Q. Wang and J. H. Li, *J. Phys. Chem. C*, 2007, **111**, 1675–1682.

58 C. F. Zhang, Z. Y. Wang, Z. P. Guo and X. W. Lou, *ACS Appl. Mater. Interfaces*, 2012, **4**, 3765–3768.

59 L. C. Yang, S. N. Wang, J. J. Mao, J. W. Deng, Q. S. Gao, Y. Tang and O. G. Schmidt, *Adv. Mater.*, 2013, **25**, 1180–1184.